



Article

Forging Treatment Realized the Isotropic Microstructure and Properties of Selective Laser Melting GH3536

Shuai Huang *, Tianyuan Wang, Kai Li, Biao Zhou, Bingqing Chen * and Xuejun Zhang

3D Printing Research and Engineering Technology Center, Beijing Institute of Aeronautical Materials, Beijing 100095, China; wangtianyuan997@foxmail.com (T.W.); kigerlee@163.com (K.L.); zhoubiao0317@163.com (B.Z.); zhangxuejun621@163.com (X.Z.)

* Correspondence: hshuai987@163.com (S.H.); hwtkjcbq1984@163.com (B.C.)

Abstract: The anisotropy of mechanical properties in SLMed alloy is very important. In order to realize the homogeneity of the microstructure and mechanical properties of GH3536 alloy prepared by selective laser melting (SLM), the as-deposited samples were treated by hot isostatic pressing and then forged at different temperatures. The microstructure, grain size, room- and high- temperature tensile properties, and endurance properties of the samples were studied. The results showed that the microstructure of the sample was mainly equiaxed austenite phase, and granular carbides were precipitated inside the grains after forging treatment, resulting in the anisotropy of the sample almost disappearing. The grain boundary phase difference distribution was most concentrated at 60°. The grain size was less than 10 µm, and a large number of twins were formed. With the increase in forging temperature, the yield strength, tensile strength, and contraction of area of the samples changed little, and the properties parallel to the z-axis (parallel samples) and vertical to the z-axis (vertical samples) were almost the same. In particular, the yield strength, tensile strength, and contraction of area in the transverse and vertical samples were almost at the same level. Judging from the elongation after fracture and the contraction of area, the properties of the samples showed characteristics of anisotropy after a high temperature endurance test.

Keywords: selective laser melting; forging treatment; GH3536 alloy; microstructure; tensile property; endurance performance



Citation: Huang, S.; Wang, T.; Li, K.; Zhou, B.; Chen, B.; Zhang, X. Forging Treatment Realized the Isotropic Microstructure and Properties of Selective Laser Melting GH3536. *J. Manuf. Mater. Process.* **2023**, *7*, 213. <https://doi.org/10.3390/jmmp7060213>

Academic Editors: Hamed Asgari and Elham Mirkoohi

Received: 2 November 2023

Revised: 25 November 2023

Accepted: 27 November 2023

Published: 29 November 2023



Copyright: © 2023 by the authors. Licensee MDPI, Basel, Switzerland. This article is an open access article distributed under the terms and conditions of the Creative Commons Attribution (CC BY) license (<https://creativecommons.org/licenses/by/4.0/>).

1. Introduction

An aero engine is an important manifestation of technological and industrial power, and its core material is the superalloy [1–3]. The performance of the superalloy directly determines the thrust-to-weight ratio and thermal efficiency of the engine. The special composition and microstructure of superalloys enable them to have high strength, excellent structural stability, outstanding fatigue resistance, and excellent oxidation resistance in high-temperature environments [4–7]. Superalloys are currently key structural materials that cannot be replaced by high-temperature parts of military and civil aero engines [8].

SLM is an advanced laser material manufacturing technology based on the basic principles of rapid prototyping. It utilizes a designed 3D slicing model to plan the laser scanning path. By melting and stacking layer by layer, it ultimately forms metal components with good properties through suitable powder and processing parameters. Metallic powders play an important role in the research of selective laser melting (SLM) forming technology [9]. At present, there are various types of materials, mainly including alloy powder, pure metal powder, and composite materials. GH3536 alloy, also known as Hastelloy X alloy, is a nickel-based high-temperature alloy which contains solid solution strengthening elements such as iron, chromium, and molybdenum, has good oxidation, corrosion resistance, and formability at high temperatures, and is often used in the forms of thin strips, plates, pipes, etc. [10]. This alloy has a certain degree of persistent hardness and creep toughness at 900 °C, with good hot working formability and welding performance. It can

also be used for short periods of time at temperatures exceeding 1080 °C [11]. Therefore, it is commonly used in high-temperature turbine and aircraft cabin heater applications. The traditional process of preparing GH3536 has high costs and technical difficulties [12]. Fortunately, using SLM technology to prepare GH3536 parts is expected to break through the traditional processing difficulties.

SLM technology can directly form metal components with complex structures. If SLM technology can be successfully applied to the commercial production and preparation of GH3536 alloy components, it can greatly promote the development of the aviation industry [13]. This paper chooses to study the SLM forming of the GH3536 alloy in order to provide a basic reference for the subsequent SLM forming of this alloy. However, due to the fact that alloy powder needs to complete melting, solidification, and cooling within a specific and extremely short interaction time during the SLM forming, a localized heat input causes extremely high temperature gradients and large residual stresses generated during the solidification process, which can lead to structural defects and component segregation [6,14–16]. Therefore, SLMed parts usually require post-heat treatment to repair internal defects, regulate the composition and structure of the microstructure, and improve the mechanical properties [17]. The main challenges faced in producing Ni-based superalloys using SLM technology include defects caused by the process, segregation, and anisotropy of mechanical properties. There is relatively little research on the anisotropy of the mechanical properties in SLMed GH3536 alloy, and also few reports on comparative research combined with heat treatment [18].

Currently, many researchers have also achieved isotropy through post-treatment methods such as heat treatment and hot isostatic pressing. The recrystallized microstructures in specimens were dependent on a distribution of refined, acicular precipitated δ phase along grain boundaries. Optimizing the process parameters to achieve consistent and defect-free multi-melt tracks and controlling porosity formation are essential. Furthermore, there is an urgent need to explore new alloys that can be processed by SLM with high quality and performance [19–21]. However, there has been no research on the high-temperature properties of materials, especially their high-temperature endurance properties. As a high-temperature alloy, the high-temperature performance of GH3536 is extremely important. Therefore, this work adopted a new composite method to achieve isotropy, and also analyzed high-temperature performance behavior. GH3536 material is suitable for manufacturing aviation engine combustion chamber components and other hot-end components that are used for a long time below 900 °C. With the increasing complexity of component structural design, traditional manufacturing processes are difficult to process and rely on additive manufacturing. After heat treatment, the performance of additive manufacturing GH3536 is difficult to meet the requirements of forging standards. Therefore, a new way to improve the performance of additive manufacturing GH3536 is explored by using additive manufacturing followed by forging, providing a performance basis for the subsequent use of complex additive GH3536 parts. The microstructure and crystallographic texture of the SLMed GH3536 samples after forging at different temperatures were characterized, and the anisotropy and its causes were discussed in combination with mechanical properties and fracture morphology. Meanwhile, the influence of forging treatment on the anisotropy of GH3536 was analyzed. The research results provide reference for the practical application of the GH3536 alloy.

2. Experimental Procedure

GH3536 powder was selected as the forming material, which was provided by the Beijing Institute of Aeronautical Materials [19]. The chemical composition is shown in Table 1. The powder particles have good sphericity and satellite balls on the surface. The average particle size was 30.0 μm . The powder was baked in a drying oven for 12 h at 90 °C to remove moisture, improve the powder flowability during laying process, and reduce oxygen content.

Table 1. Chemical composition of GH3536 powder (wt.%).

Cr	Fe	Mo	W	Mn	Cu	C	Si	S	Ni
22.710	18.750	8.940	2.110	0.007	0.031	0.076	0.130	0.001	Bal.

The SLM forming equipment was EOS290. To prevent oxidation, the entire SLM process was carried out in an argon environment. The main process parameters were: laser power 260 W, scanning speed 1100 mm/s, and scanning spacing 110 μm . The minimum layer thickness was 40 μm , the interlayer scanning angle was 67°, and the printed sample size was 60 mm \times 60 mm \times 90 mm. According to the alloy characteristics, the previously printed formed parts were subjected to post-treatment using HIP. The specific process was as follows: the heating rate 5 °C/min, the temperature 1050 °C, and the pressure 120 MPa. The insulation was kept for 3 h, and the furnace was cooled with N₂ atmosphere.

After HIP treatment, the forging treatment proceeded. Specifically, the sample surface was covered and placed on the rack to avoid touching the furnace bottom plate. These samples were put into the furnace at room temperature, heated to the forging temperature, and kept for 1 h before being taken out of the furnace for forging. The diameter of the flat mold was Φ 400 mm, the forging temperature was 1050 °C, 1080 °C, and 1100 °C, and air cooling after forging occurred according to Table 2. The basic reason for choosing the forging temperature was that the solid solution temperature of GH3536 was 1175 °C. To ensure the solid solution strengthening effect, choosing a deformation temperature lower than the solid solution temperature could obtain a relatively fine grain size. The forging temperature ranging from 1050 °C to 1100 °C was to study the trend of grain size and the dynamic recrystallization ratio during the forging deformation process. The lower the temperature, the finer the grain size could be obtained at 1050 °C. The higher the temperature, the higher the dynamic recrystallization ratio. The samples that were forged parallel to the z-axis were named parallel samples, and the samples that were forged vertical to the z-axis were named vertical samples. The room-temperature and high-temperature properties of the samples before forging are shown in Table 3.

After forging, parallel and vertical samples were polished with sandpapers and a diamond polishing agent. The polished samples were subjected to metallographic corrosion using reagent (with a volume ratio of HNO₃ and HCl of 1:3) for 10 s. The microstructure was observed through an optical microscopy (OM), a scanning electron microscopy (SEM), and an energy dispersive spectroscopy (EDS). Electrolytic polishing was performed on mechanically polished samples using a volume fraction of 5% perchloric acid, and the working distance was 18.5 mm while the detector distance was 20 mm. Tensile tests on the parallel and vertical samples were conducted at a rate of 0.5 mm/min at room temperature and 650 °C according to the ASTM E1856-13(2021) [22], and the fracture surface was observed by SEM.

Table 2. The parameters of forging treatment for SLMed samples after HIP.

No.	Size /mm ³	Forging Temperature/°C	Deformation Velocity/mm/s	Deformation Amount/mm	Forging Direction
1#	60 \times 60 \times 90	1050	20	<i>H</i> = 90 mm forging to <i>H</i> = 36 mm	Parallel to z-axis
2#	60 \times 60 \times 90				Vertical to z-axis
3#	60 \times 60 \times 90	1080			Parallel to z-axis
4#	60 \times 60 \times 90				Vertical to z-axis
5#	60 \times 60 \times 90	1110			Parallel to z-axis
6#	60 \times 60 \times 90				Vertical to z-axis

Table 3. Room-temperature and high-temperature properties of samples before forging.

Samples	Temperature /°C	Tensile Strength /MPa	Yield Strength /MPa	Elongation /%	Contraction of Area/%
Vertical to the z-axis	23	726	305	49.4	45.9
Parallel to the z-axis		721	313	53.9	57.7
Vertical to the z-axis	650	520	185	46.4	40.6
Parallel to the z-axis		532	192	51.8	50.9
Vertical to the z-axis	815	336	175	47.2	45.8
Parallel to the z-axis		342	186	42.6	40.5

3. Results and Discussion

3.1. Microstructure and Composition of Samples after Forging

Figure 1 shows the microstructure of samples after forging at 1050 °C. After forging treatment, the original pool morphology and laser scanning traces completely disappeared, and it was difficult to observe cellular and columnar subgrains, which were replaced by the formation of equiaxed grains, indicating that grain recrystallization occurred during forging. Defects such as cracks were often found in the deposited samples that were completely eliminated after HIP and forging. Comparing the microstructures parallel to the z-axis and vertical to the z-axis and their corresponding components, it was found that the forging treatment basically eliminated the anisotropy of the microstructure. The element contents in the GH3536 were similar in both directions (Table 4). The main elements, such as Cr, Fe, Mo, and Co, were the same as that of the base metal powder. Due to the small difference in chemical composition, the GH3536 alloy prepared under the same forging conditions had similar microstructures. Equiaxed grains were formed in the samples parallel to the z-axis and vertical to the z-axis.

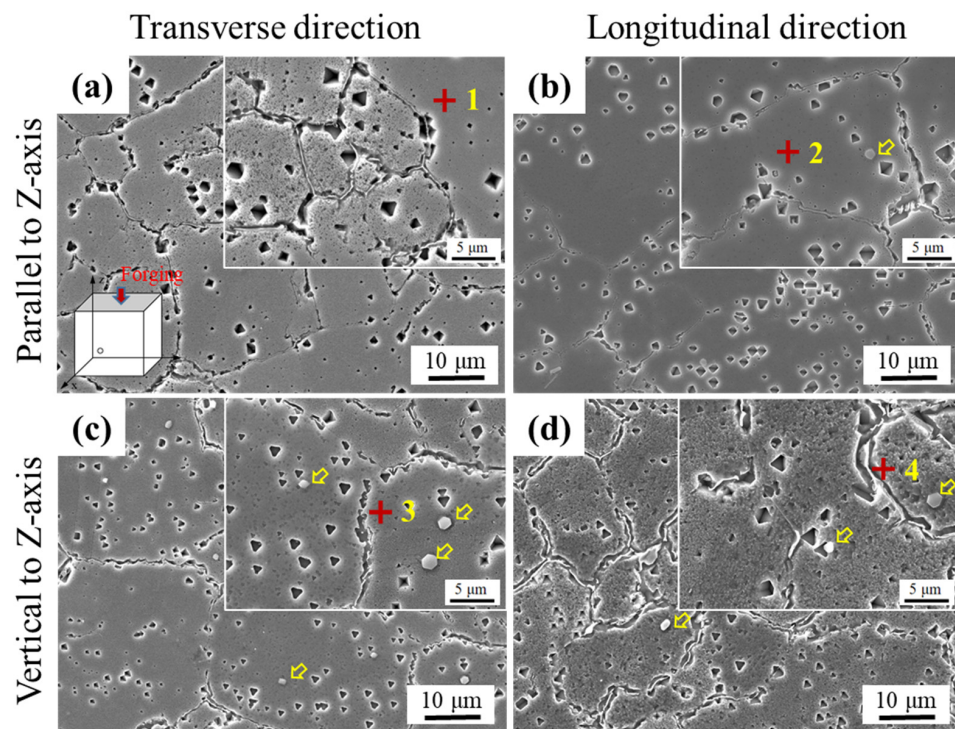


Figure 1. Microstructure at forging temperature of 1050 °C: (a) transverse observation parallel to the z-axis; (b) longitudinal observation parallel to the z-axis; (c) transverse observation vertical to the z-axis; (d) longitudinal observation vertical to the z-axis.

Table 4. The elements and components corresponding to the observation position in Figure 1.

Point	Cr	Fe	Co	Ni	Mo	W
1	38.94	13.64	1.26	29.99	14.65	1.51
2	25.31	17.77	1.79	43.81	10.25	1.07
3	37.66	14.17	1.29	31.42	14.1	1.36
4	35.99	14.44	1.41	32.82	13.99	1.34

The microstructure after forging showed that there were precipitates in the grain and grain boundary. Some precipitates were distributed along the grain boundary and were connected to each other in a chain shape, which had an adverse effect on the performance. Some precipitates inside the grains were dispersed and connected to the precipitates of the layer, which was beneficial to improve the mechanical strength. The room-temperature microstructure of the GH3536 superalloy was mainly an austenite structure. After rapid solidification by SLM and the high-temperature slow cooling process of heat treatment and HIP, carbides such as $M_{23}C_6$, M_6C , and σ would be precipitated [23–26]. Spherical carbides were dispersed in the grains, and a large number of block carbides were distributed at the grain boundaries.

When the forging temperature was 1080 °C, punctate carbide precipitates formed along the grain boundary (Figure 2 and Table 5). Combined with the research of Montero-Sistiaga et al., it was found that the precipitated phase was $M_{23}C_6$ [27,28]. The solubility of C atoms in γ -Ni was limited, so it was segregated in the grain boundary region. The C atoms at the grain boundary and the surrounding M atoms (mainly Cr) formed carbide precipitates. With the increase in the solution temperature, the diffusion ability of atoms was enhanced, and the formed $M_{23}C_6$ carbide had the phenomenon of re-dissolution.

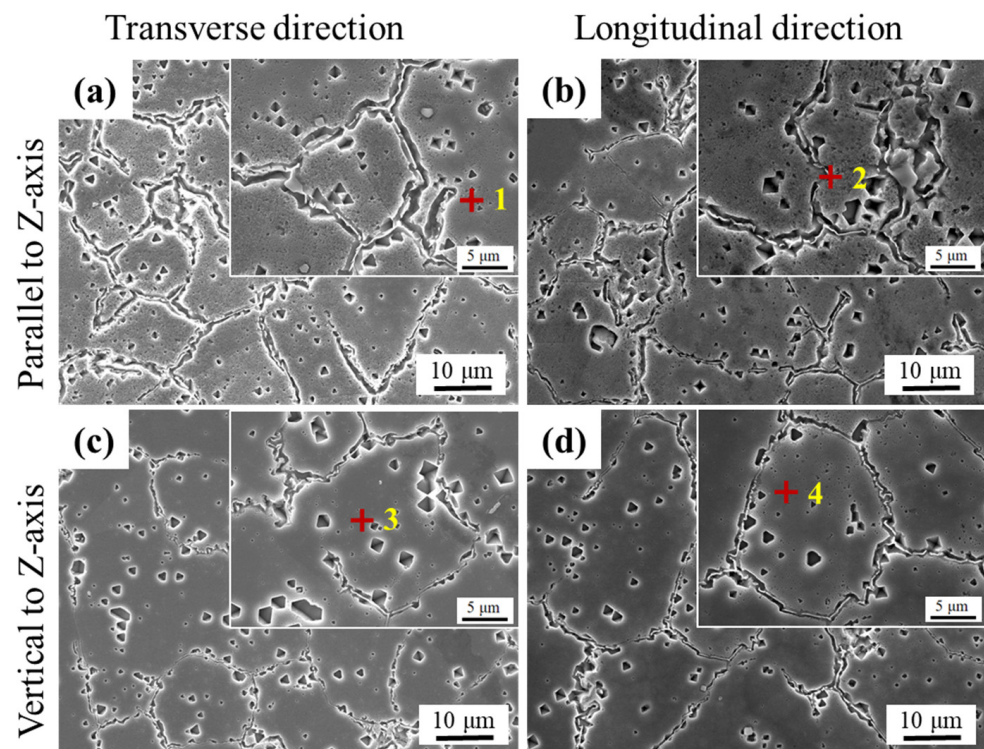


Figure 2. Microstructure at forging temperature of 1080 °C: (a) transverse observation parallel to the z-axis; (b) longitudinal observation parallel to the z-axis; (c) transverse observation vertical to the z-axis; (d) longitudinal observation vertical to the z-axis.

Table 5. The elements and components corresponding to the observation position in Figure 2.

Point	Cr	Fe	Co	Ni	Mo	W
1	36.1	14.48	1.4	32.86	13.78	1.38
2	32.56	15.49	1.49	35.98	13.22	1.26
3	25.42	15.8	1.53	37.65	9.87	0.98
4	24.3	18.24	1.82	45.31	9.29	1.03

When the forging temperature was 1100 °C, the dissolution of carbides was incomplete, the presence of carbides hindered the migration of grain boundaries, and the grain size was small (Figure 3 and Table 6). If the forging temperature continued to increase, the degree of dissolution of the carbides distributed at the grain boundary increased, and the pinning of carbides on the grain boundary weakened, which reduced the resistance of grain growth. The thermal activation process led to a decrease in the interfacial free energy, which promoted grain boundary migration, and the thermal activation process further coarsened grains.

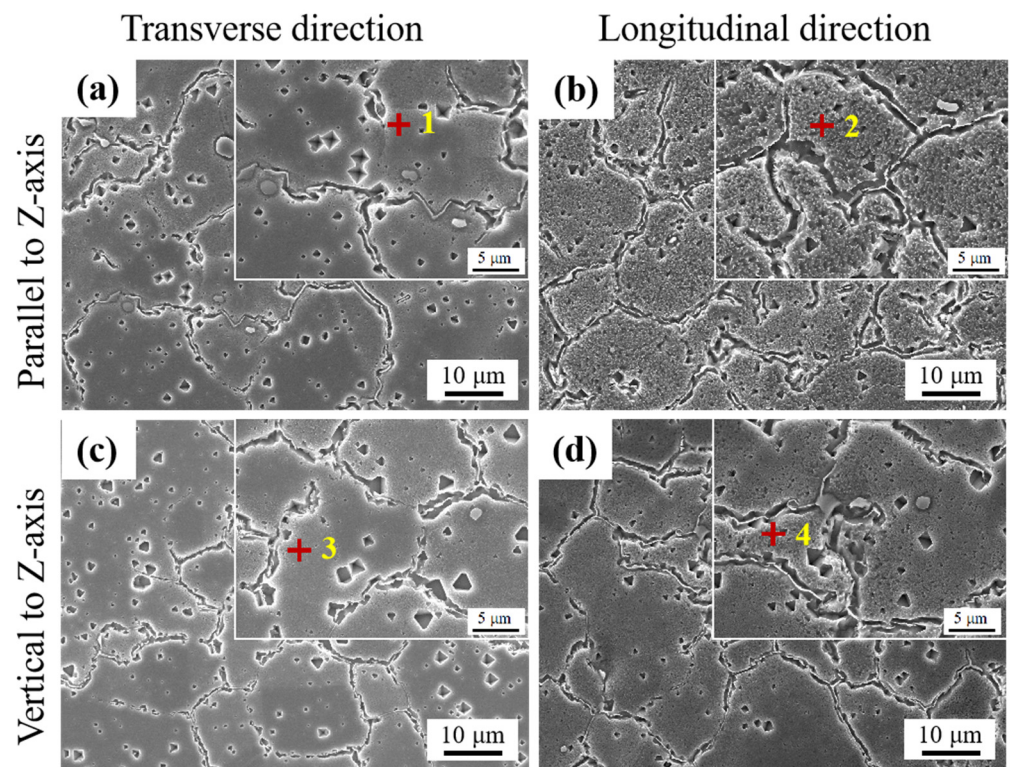


Figure 3. Microstructure at forging temperature of 1100 °C: (a) transverse observation parallel to the z-axis; (b) longitudinal observation parallel to the z-axis; (c) transverse observation vertical to the z-axis; (d) longitudinal observation vertical to the z-axis.

Table 6. The elements and components corresponding to the observation position in Figure 3.

Point	Cr	Fe	Co	Ni	Mo	W
1	31.45	15.96	1.43	37.14	12.77	1.26
2	30.51	16.13	1.54	38.01	12.54	1.28
3	28.52	17.19	1.68	40.65	10.94	1.02
4	38.07	13.82	1.3	30.92	14.55	1.34

3.2. Grains of Samples after Forging

In order to research the influence of different forging temperatures on the grain size of samples, EBSD characterization was carried out. Figure 4 shows the grain characteristics of

parallel samples at different forging temperatures. Combined with EBSD results, the degree of grain equiaxedness was significantly improved. After forging at 1050 °C, significant annealing twins were found. The grain size of samples was mostly concentrated within 12 μm, with an average value of 13.3 μm. The grain boundary phase difference was distributed between 2 and 60°, of which 60° was the most concentrated. Therefore, the deformed grains and twins in the microstructure were the main grains.

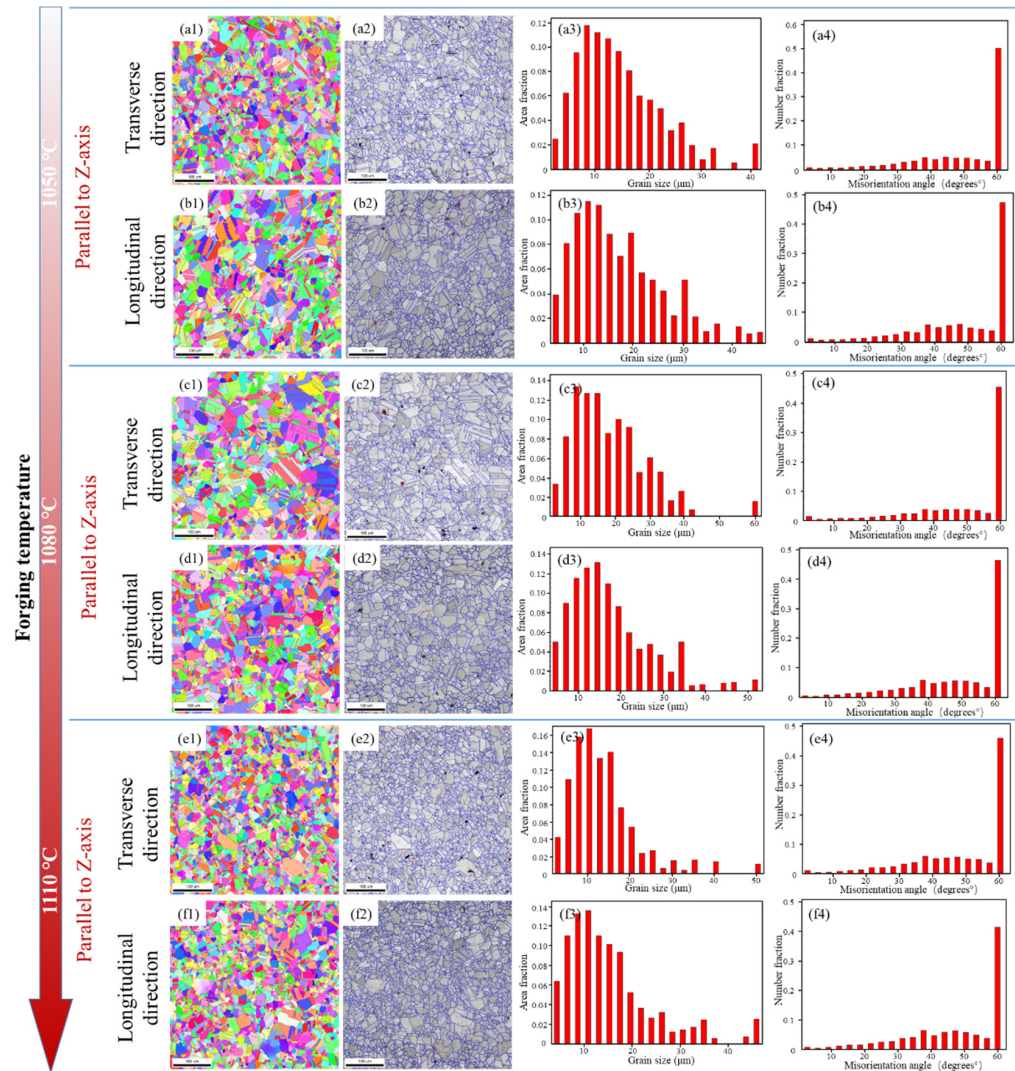


Figure 4. The grain size and its distribution parallel to the z-axis at different forging temperatures: forging temperature 1050 °C, (a1–a4) transverse observation, and (b1–b4) longitudinal observation; forging temperature 1080 °C, (c1–c4) transverse observation, and (d1–d4) longitudinal observation; forging temperature 1110 °C, (e1–e4) transverse observation, and (f1–f4) longitudinal observation.

When the sample was forged at 1050 °C, the crack defects in the microstructure disappeared, and there was no obvious defect feature. After forging at 1080 °C, the microstructure had changed, the number of recrystallized grains increased, and the grains were further refined. The number of irregular equiaxed grains increased, and the grain size was not uniform. Some equiaxed grains were interspersed. When the sample was forged at 1100 °C, the microstructure was further transformed, and the grains became extremely fine and uniform. At this time, the grain size was mostly concentrated within 9 μm, with an average value of 10.3 μm. The grain boundary phase difference distribution was most concentrated at 60°. After the sample was treated at 1050 °C, the degree of grain homogenization further deepened, but the effect was not significantly improved. After

being treated at 1080 °C, the size difference between large and small grains decreased, and the grain size in the microstructure tended to evolve towards uniformity. The grain morphology began to become regular, and the appearance of irregularly shaped grains began to decrease. After the sample was treated at 1100 °C, the number of newly formed grains increased after recrystallization, and the size of the remaining large grains tended to be basically consistent, presenting finer grains.

Figure 5 shows the grain characteristics of vertical samples at different forging temperatures. After forging at 1050 °C, significant annealing twins could be found, and the grain size was mostly concentrated within 10 μm, with an average of 13.3 μm. The grain boundary phase difference was distributed between 10 and 60°. When the sample was forged at 1100 °C, the grains became fine and uniform. The grain size of the sample was mostly concentrated within 10 μm. Compared with the grain characteristics of the parallel samples, the grain size and distribution in the two directions were almost the same, and the distribution of the grain boundary phase difference had no obvious change, indicating that the grain structure showed the same results.

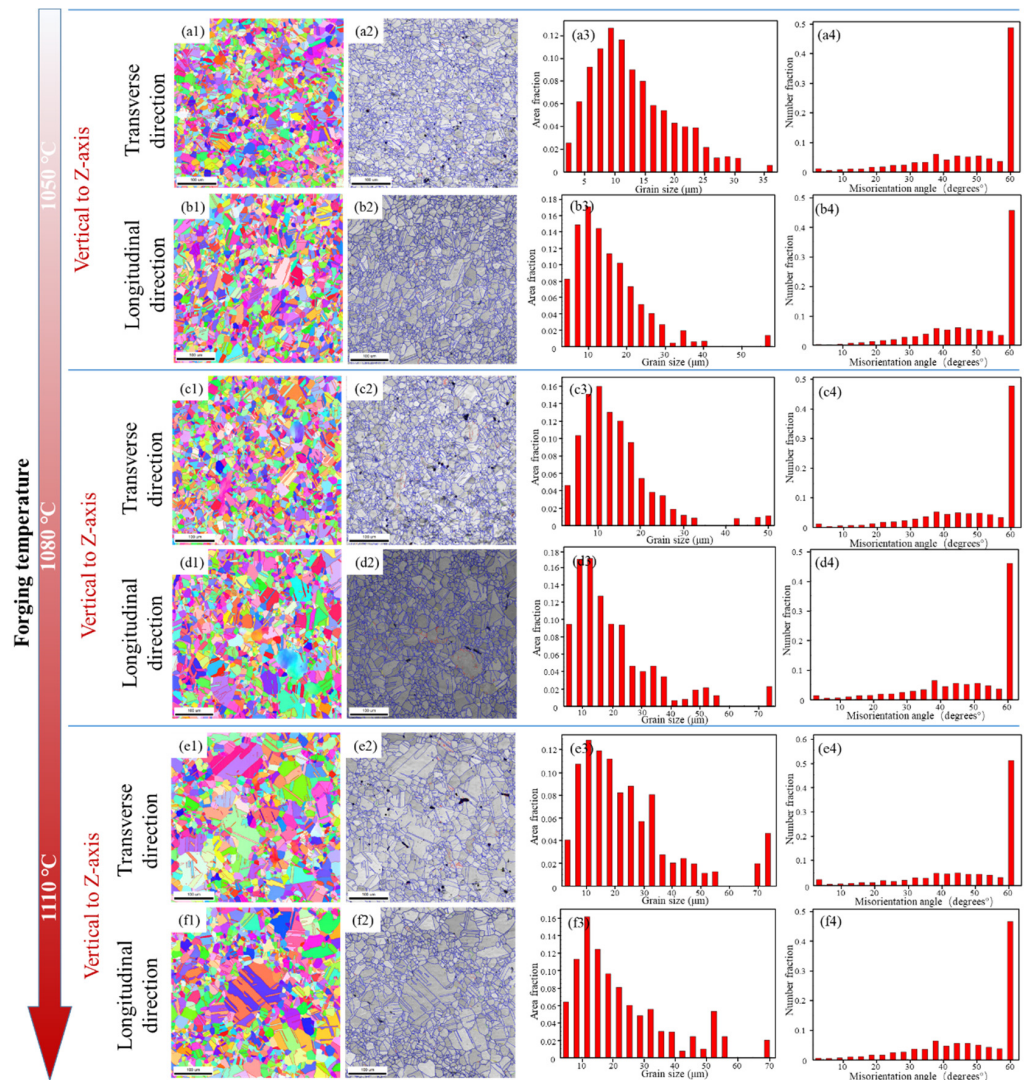


Figure 5. The grain size and its distribution vertical to the z-axis at different forging temperatures: forging temperature 1050 °C, (a1–a4) transverse observation, and (b1–b4) longitudinal observation; forging temperature 1080 °C, (c1–c4) transverse observation, and (d1–d4) longitudinal observation; forging temperature 1110 °C, (e1–e4) transverse observation, and (f1–f4) longitudinal observation.

3.3. Room-Temperature Tensile Properties of Samples

The room-temperature tensile properties of samples after forging are shown in Figure 6. With the increase in forging temperature, the yield strength, tensile strength, and contraction of area of the samples changed little, and the properties of the parallel and vertical samples were almost the same. The average tensile properties of vertical samples were: yield strength 352 MPa, tensile strength 795 Mpa, elongation 47%, and contraction of area 64%.

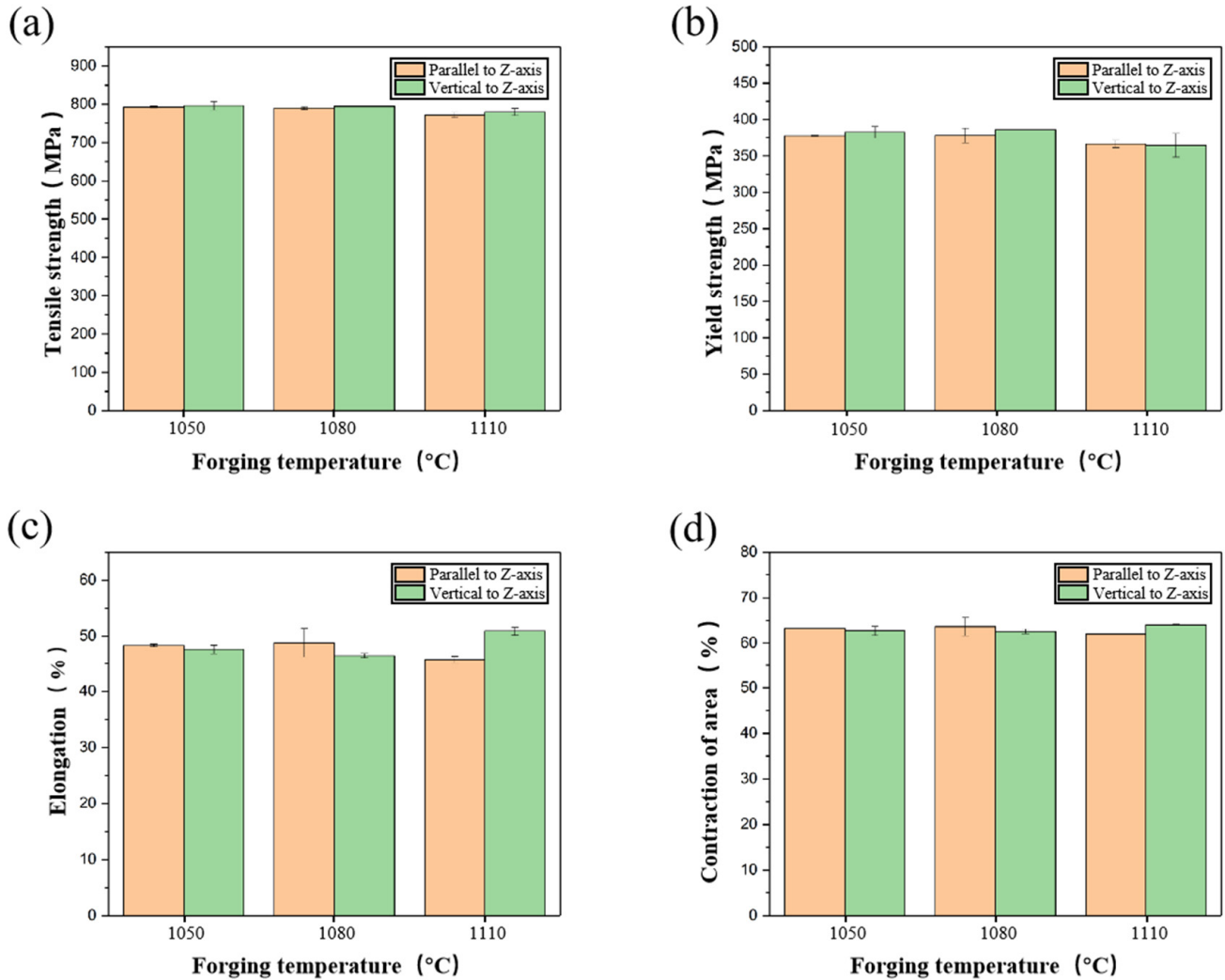


Figure 6. Room-temperature properties of samples after forging at different temperatures: (a) tensile strength; (b) yield strength; (c) elongation; (d) contraction of area.

It should be pointed out that there was obvious anisotropy in the strength and toughness of parallel and vertical samples after deposition. The tensile properties of samples after forging treatment were basically isotropic in the parallel and vertical directions. It was found that the yield strength of the forged sample was significantly lower than that of the deposited sample, while the elongation after fracture increased. This was mainly due to the change in grain boundary morphology and the elimination of defects. On the one hand, the sub-grains in the deposited samples could be regarded as LAGBs during the deformation process, which played a role in grain boundary strengthening [29]. After forging, the subgrain structure in the crystal disappeared, which led to the weakening of grain boundary strengthening and the decrease in yield strength. On the other hand, the cracks were closed after forging treatment, the number of pore defects was reduced, and the density was improved [30]. At the same time, the heat treatment eliminated some residual stress, and finally the yield strength of the forging sample was reduced and the toughness

was improved. After forging treatment, the original fish-scale molten pool and columnar crystal structure of the sample were almost completely eliminated, thus obtaining the ideal homogeneity.

Figure 7 shows the room-temperature tensile fracture morphology of parallel samples after forging treatment. The number of room-temperature fracture cracks of the parallel sample was reduced, the material compactness was improved, and the forging effect was obvious. The morphology was uneven and had obvious tearing marks. At high magnification, it was mainly characterized by dimples, showing an obvious ductile fracture mode. Forging treatment improved the plasticity of the material. In addition, the comparison of the room-temperature tensile fracture morphology of the vertical and parallel samples after forging showed that the low-magnification fracture morphology and the high-magnification fracture morphology were similar (Figure 8). This phenomenon corresponded to the room-temperature tensile mechanical property of samples after forging, which further illustrated that the anisotropic characteristics disappeared after forging. Ref. [31] found that 20–50 nm nano-oxide particles had a measurable and detrimental effect on the fracture properties of materials. The precipitated carbides in this work had similar fracture morphology.

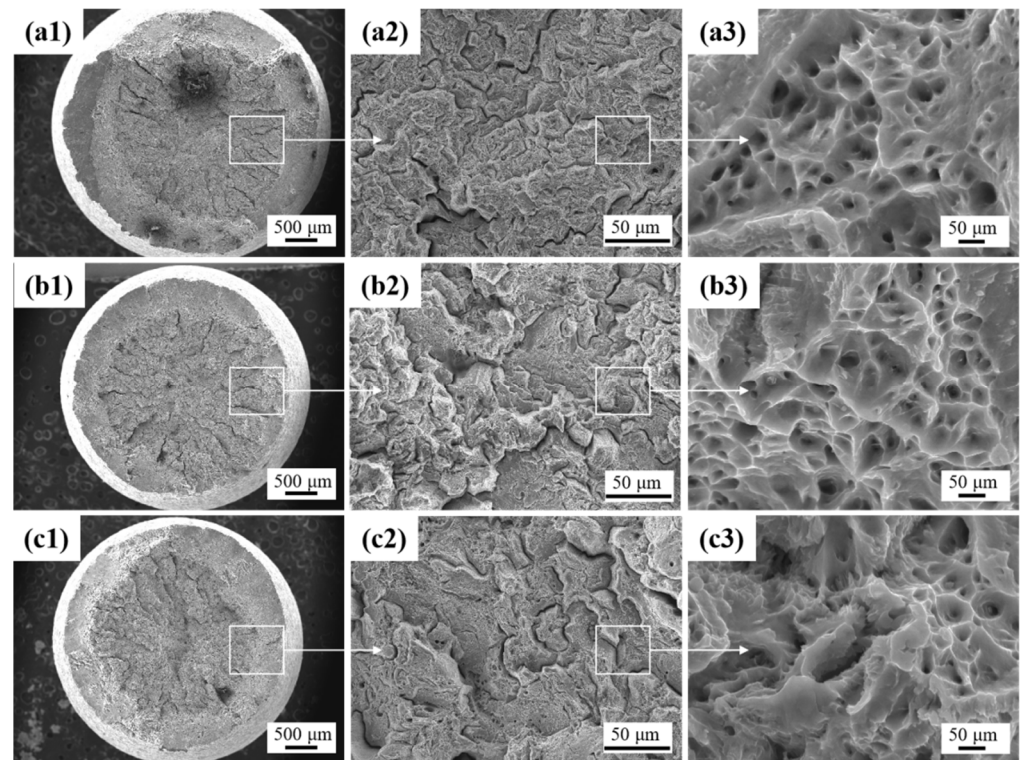


Figure 7. Fracture analysis of room-temperature mechanical properties of vertical samples at different forging temperatures: (a1–a3) 1050 °C, (b1–b3) 1080 °C, (c1–c3) 1110 °C.

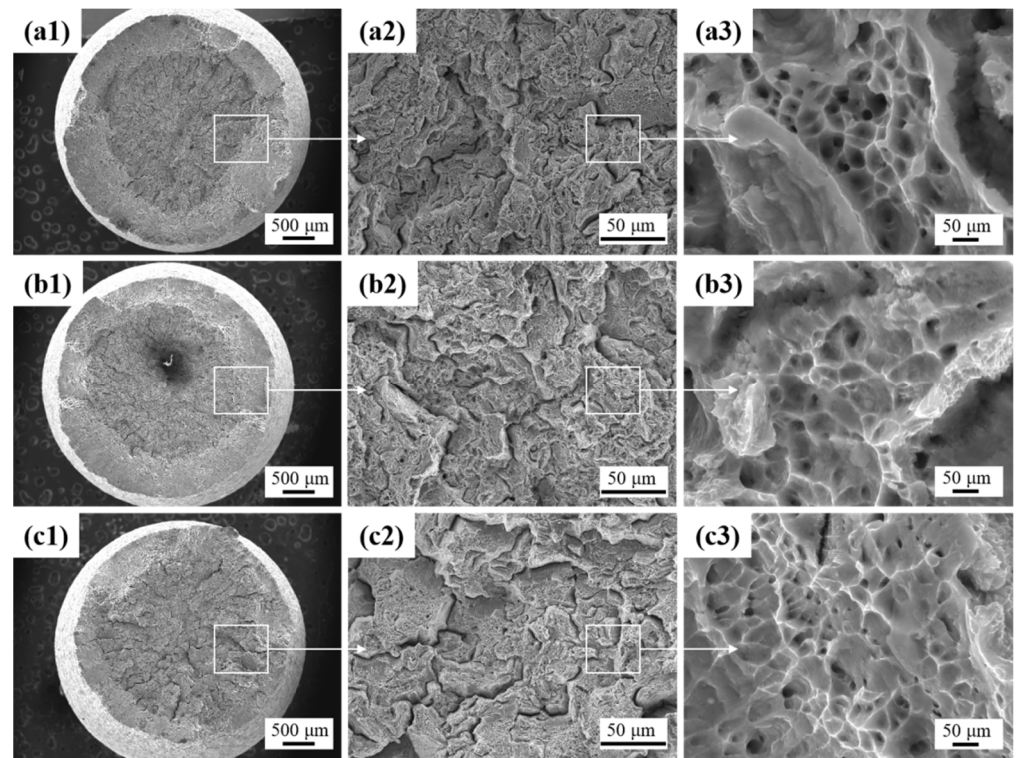


Figure 8. Fracture analysis of room temperature mechanical properties of parallel samples at different forging temperatures: (a1–a3) 1050 °C, (b1–b3) 1080 °C, (c1–c3) 1110 °C.

3.4. High-Temperature Properties of Samples after Forging

3.4.1. High-Temperature Tensile Property

The high-temperature tensile properties of samples after forging are tested at 650 °C, and the results are shown in Figure 9. In order to research the effect of forging treatment on anisotropy, tensile samples were prepared along the parallel and vertical directions for high-temperature mechanical properties testing. The comparison showed that the as-deposited samples had obvious anisotropy. The tensile strength in the vertical direction was higher than that in the parallel direction, but the elongation was lower, which was determined by the force direction of columnar crystal. During vertical tension, the dislocation had a small movement space in the crystal, which was hindered by high-density grain boundaries, forming a high yield strength. When the parallel tension was applied, the dislocation motion space was large, and the continuous deformation ability was good, so as to obtain better elongation.

The equiaxed grains replaced the columnar grains, resulting in the anisotropy of samples almost disappearing after forging treatment. In particular, the yield strength, tensile strength, and contraction of area in the parallel and vertical samples were almost the same level at three temperatures. In addition, compared with the deposited samples, the forged samples showed low strength and high plasticity in a high-temperature tensile test.

After forging treatment, the carbides distributed along the grain were eliminated, and the combination of intragranular carbide dispersion strengthening and solid solution strengthening improved ultimate tensile strength and elongation. Under the condition of 650 °C, the elongation in the vertical samples increased, which was closely related to the transformation of the cellular subgrain structure and precipitated phase in the crystal. At the same time, the grain coarsening further extended the dislocation slip distance, resulting in forged samples that generally had better tensile plasticity.

Figure 10 is the high-temperature tensile fracture morphology of vertical samples after forging treatment. Compared with the high-temperature tensile fracture morphology of the deposited samples, the number of cracks in the high-temperature fracture morphology

of the forged sample was significantly lower, and the compactness of the material was improved.

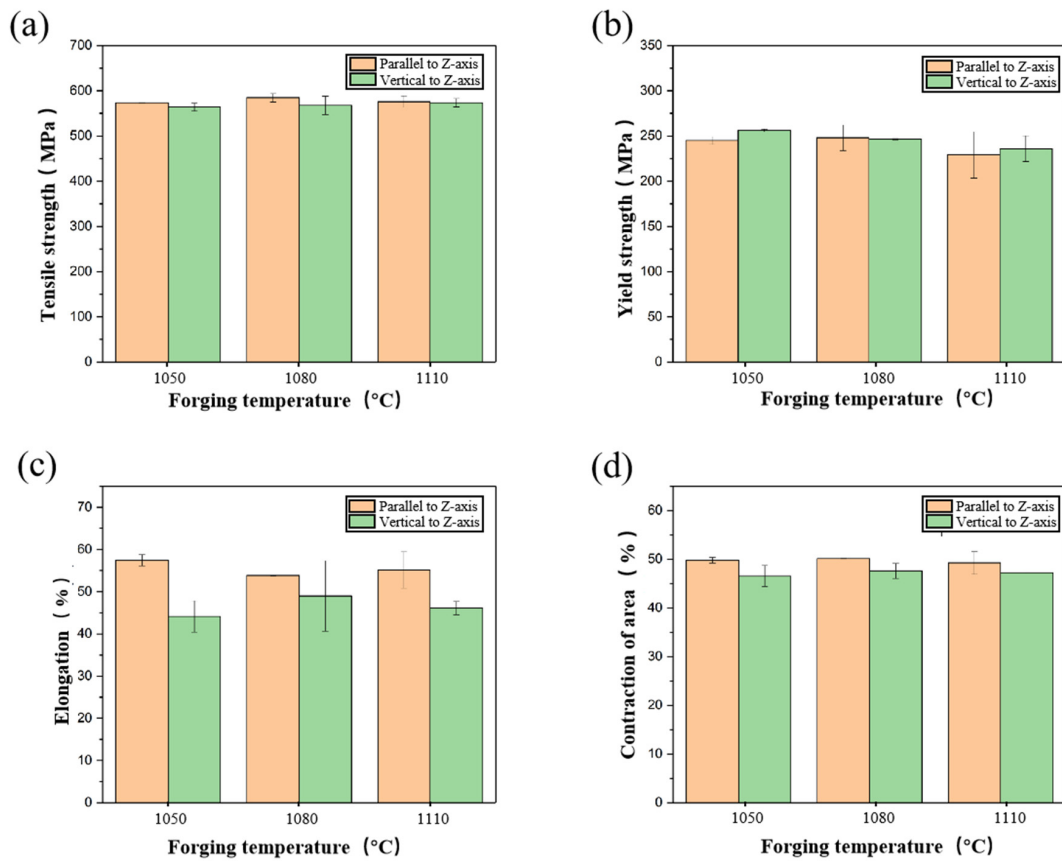


Figure 9. High-temperature mechanical properties of samples after forging at different temperatures: (a) tensile strength; (b) yield strength; (c) elongation; (d) contraction of area.

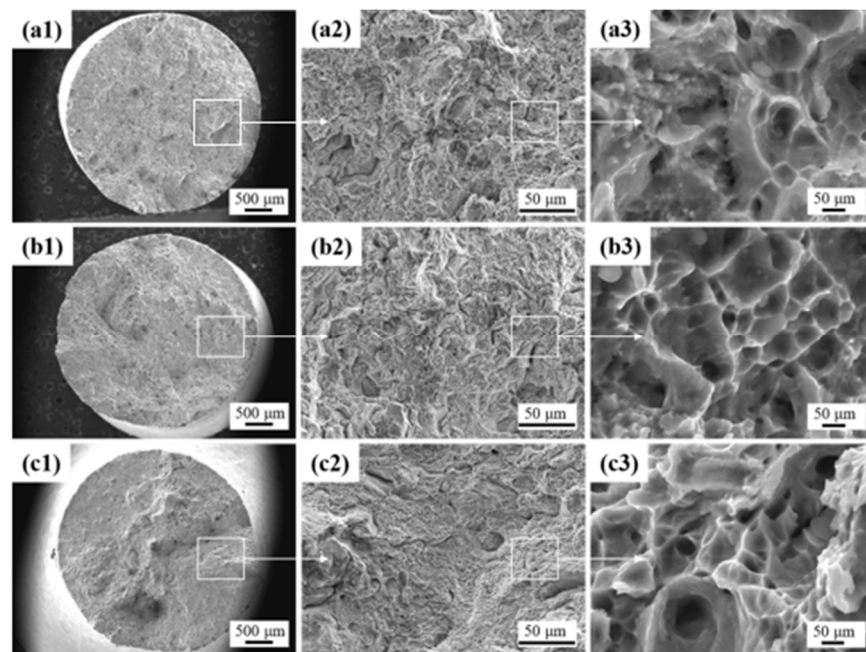


Figure 10. Fracture analysis of high-temperature mechanical properties of vertical samples at different forging temperatures: (a1–a3) 1050 °C, (b1–b3) 1080 °C, (c1–c3) 1110 °C.

The high-temperature fracture morphology of the forged sample in the vertical direction was relatively deposited, and had dimple characteristics. The fracture mechanism was a high-temperature ductile fracture, which was obviously compared with the river-like pattern in the high-temperature fracture morphology of the deposited sample and the high-temperature brittle fracture mode. After forging treatment, the high-temperature plasticity of the sample was greatly enhanced, which corresponded to the high-temperature tensile strength.

In addition, by comparing the high-temperature fracture morphology of the forged vertical and parallel samples, the high-temperature fracture morphology was similar, which corresponded to the high-temperature tensile (Figures 10 and 11). It showed that the high-temperature properties of the vertical and parallel samples were close to each other after forging treatment.

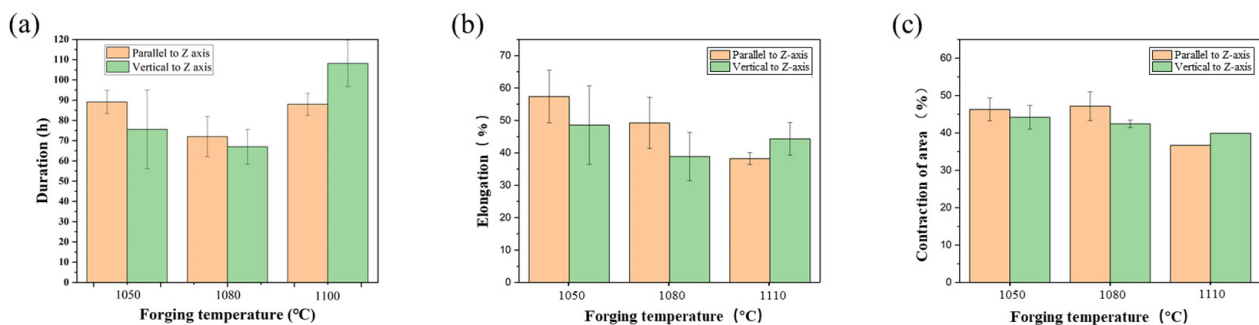


Figure 11. High-temperature endurance property of samples after forging at different temperatures: (a) duration time; (b) elongation; (c) contraction of area.

When the GH3536 alloy was stretched at high temperature, an intergranular fracture occurred. This was because with the increase in tensile temperature, the strength of the grain interior and grain boundary decreased, and the strength of the grain boundary was lower than that of the grain interior at 650 °C. There were relatively many holes and metallurgical defects near the grain boundary, which made it easier for atoms at the grain boundary to diffuse at high temperature, and the decrease rate of grain boundary strength was higher than that of crystal. The micron-sized carbides distributed at the grain boundaries caused stress concentration, which accelerated the fracture of the forging sample and made it have lower ultimate tensile strength and elongation at a high temperature.

3.4.2. High-Temperature Endurance Property

The endurance performance of samples under stress conditions of 340 MPa and a temperature of 650 °C is shown in Figure 11. After forging treatment at a temperature of 1050 °C, the duration of parallel and vertical samples was 89 h and 77 h, respectively. After forging treatment at 1080 °C, the duration of the parallel and vertical samples was 75 h and 70 h, respectively. After forging treatment at a temperature of 1100 °C, the duration of parallel and vertical samples was 90 h and 110 h, respectively. As the forging temperature increased from 1050 °C to 1100 °C, the elongation of parallel samples gradually decreased from 56% to 41%. The elongation of vertical samples showed fluctuation, decreasing from 50% to 40% and then increasing to 45%. The cross-sectional shrinkage of parallel samples showed a decreasing trend with the increase in forging temperature, and the cross-sectional shrinkage of vertical and parallel samples were different. Judging from the elongation and contraction of area after fracture, the performance of samples exhibited various anisotropic characteristics after high-temperature endurance.

Figure 12 shows the comparison of fracture surfaces after the high-temperature endurance testing of parallel and vertical samples after forging. There were a large number of dimples on the fracture surface, without the appearance of brittle fracture. After forging treatment, there were no obvious tensile cracks on the fracture surfaces in both samples, and a large number of dimples were generated. However, these dimples were shallow and not

sharp, and the surface of the dimple tip was smooth without obvious tearing marks during plastic stretching. The fracture morphology in both samples was not significantly different, and just judging from the morphology, the fracture exhibited isotropic characteristics.

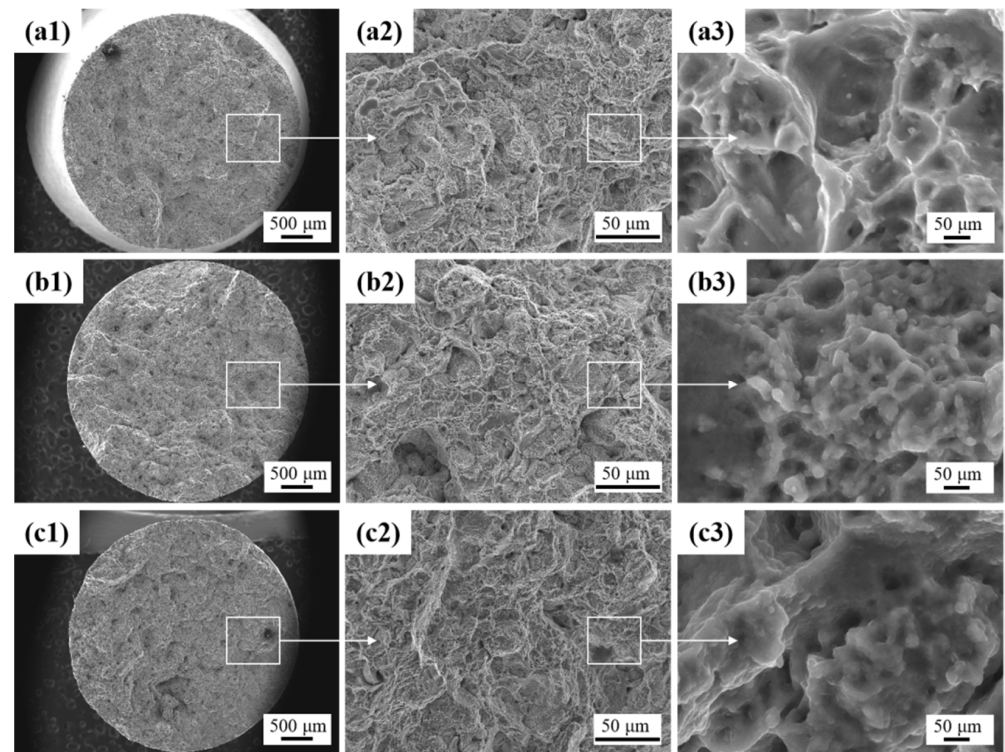


Figure 12. Fracture analysis of high-temperature endurance property of vertical samples at different forging temperatures: (a1–a3) 1050 °C, (b1–b3) 1080 °C, (c1–c3) 1110 °C.

4. Conclusions

- (1) Forging treatment eliminated the microstructure anisotropy. The microstructure parallel to the z-axis and vertical to the z-axis and their corresponding components were similar. Equiaxed grains were formed, and there were carbides in the grain and grain boundary. Spherical carbides were dispersed in the grains.
- (2) With the increase in forging temperature, the degree of equiaxed grains was significantly improved, and a large number of annealing twins were formed. The grain size was mostly concentrated within 10 μm, and the grain boundary phase difference was most concentrated at 60°.
- (3) With the increase in forging temperature, the yield strength, tensile strength, and contraction of area of the samples changed little, and the properties of parallel and vertical samples were almost the same.
- (4) The yield strength, tensile strength, and contraction of area in the parallel and vertical samples were almost the same at three temperatures. Judging from the elongation after fracture and the contraction of area, the sample properties showed anisotropy characteristics after a high-temperature endurance test at 650 °C.

Author Contributions: Conceptualization, S.H. and B.C.; data curation, B.Z. and K.L.; writing—original draft preparation, S.H. and T.W.; writing—review and editing, S.H., B.C. and X.Z.; project administration, X.Z. All authors have read and agreed to the published version of the manuscript.

Funding: This research and the APC was funded by the National Natural Science Foundation of China (Grant No. 52005465).

Data Availability Statement: Data are contained within the article.

Conflicts of Interest: The authors declare no conflict of interest.

References

1. Ohnabe, H.; Masaki, S.; Onozuka, M.; Miyahara, K.; Sasa, T. Potential application of ceramic matrix composites to aero-engine components. *Compos. Part A Appl. Sci. Manuf.* **1999**, *30*, 489–496. [[CrossRef](#)]
2. Lv, C.; Chang, J.; Bao, W.; Yu, D. Recent research progress on airbreathing aero-engine control algorithm. *Propuls. Power Res.* **2022**, *11*, 1–57. [[CrossRef](#)]
3. Wang, Y.; Guo, W.; Xie, Y.; Li, H.; Zeng, C.; Xu, M.; Zhang, H. In-situ monitoring plume, spattering behavior and revealing their relationship with melt flow in laser powder bed fusion of nickel-based superalloy. *J. Mater. Sci. Technol.* **2023**, *177*, 44–58. [[CrossRef](#)]
4. Zhao, S.; Xie, X.; Smith, G.D.; Patel, S.J. Microstructural stability and mechanical properties of a new nickel-based superalloy. *Mater. Sci. Eng. A* **2003**, *355*, 96–105. [[CrossRef](#)]
5. Wang, R.; Yang, D.; Wang, W.; Wei, F.; Lu, Y.; Li, Y. Tool wear in nickel-based superalloy machining: An overview. *Processes* **2022**, *10*, 2380. [[CrossRef](#)]
6. Wang, Y.; Guo, W.; Zheng, H.; Xie, Y.; Zhang, X.; Li, H.; Xu, M.; Zhang, H. Microstructure, crack formation and improvement on Nickel-based superalloy fabricated by powder bed fusion. *J. Alloys Compd.* **2023**, *962*, 171151. [[CrossRef](#)]
7. Chen, N.; Zheng, D.; Niu, P.; Li, R.; Yuan, T. Laser powder bed fusion of GH3536 nickel-based superalloys: Processing parameters, microstructure and mechanical properties. *Mater. Charact.* **2023**, *202*, 113018. [[CrossRef](#)]
8. Pollock, T.M.; Tin, S. Nickel-based superalloys for advanced turbine engines: Chemistry, microstructure and properties. *J. Propuls. Power* **2006**, *22*, 361–374. [[CrossRef](#)]
9. Yadroitsev, I.; Bertrand, P.; Smurov, I. Parametric analysis of the selective laser melting process. *Appl. Surf. Sci.* **2007**, *253*, 8064–8069. [[CrossRef](#)]
10. Ren, Y.; Li, Z.; Chen, Y.; Xin, Z.; Ye, Y.; Lu, H.; Wan, H.; Cheng, L.; He, K.; Tu, X. Effect of Heat Treatment on the Microstructure and Mechanical Properties of Nickel Superalloy GH3536 Obtained by Selective Laser Melting. *Met. Sci. Heat Treat.* **2021**, *63*, 369–374. [[CrossRef](#)]
11. Zhang, L.; Song, J.; Wu, W.; Gao, Z.; He, B.; Ni, X.; Long, Q.; Lu, L.; Zhu, G. Effect of processing parameters on thermal behavior and related density in GH3536 alloy manufactured by selective laser melting. *J. Mater. Res.* **2019**, *34*, 1405–1414. [[CrossRef](#)]
12. Min, S.; Zhang, H.; Liu, H.; Zhang, K.; Huang, A.; Hou, J. Influence of defects on high-temperature oxidation performance of GH3536 superalloys fabricated by laser powder bed fusion. *Addit. Manuf. Lett.* **2022**, *3*, 100064. [[CrossRef](#)]
13. Liu, M.; Liu, Z.; Li, B.; Qi, F.; Peng, W. Numerical simulation on melt pool and solidification in the direct energy deposition process of GH3536 powder superalloy. *J. Mater. Res. Technol.* **2023**, *26*, 5626–5637. [[CrossRef](#)]
14. Cui, J.; Wang, H.; Yang, Z.; Zhao, M.; Guo, Y. Study on grain boundary distribution and formation mechanism in GH3536 superalloy strip and foil after annealing treatment. *Mater. Charact.* **2022**, *192*, 112236. [[CrossRef](#)]
15. Xiao, L.; Peng, Z.; Zhao, X.; Tu, X.; Cai, Z.; Zhong, Q.; Wang, S.; Yu, H. Microstructure and mechanical properties of crack—Free Ni—Based GH3536 superalloy fabricated by laser solid forming. *J. Alloys Compd.* **2022**, *921*, 165950. [[CrossRef](#)]
16. Qiao, G.; Zhang, B.; Bai, Q.; Dilnoza, Y. Effect of heat treatment on microstructure and residual stress of GH3536 superalloy fabricated by selective laser melting. *J. Mater. Eng. Perform.* **2021**, *30*, 8892–8900. [[CrossRef](#)]
17. Yan, P.; Bai, J.; Yuan, Z.; Wang, S.; Ma, R.; Zheng, J. Constitutive Equation and Hot Deformation Behavior of SLM-GH3536 Alloy. *JOM* **2023**, *75*, 4819–4831. [[CrossRef](#)]
18. Wei, Q.; Xie, Y.; Teng, Q.; Shen, M.; Sun, S.; Cai, C. Crack Types, Mechanisms, and Suppression Methods during High-energy Beam Additive Manufacturing of Nickel-based Superalloys: A Review. *Chin. J. Mech. Eng. Addit. Manuf. Front.* **2022**, *1*, 100055. [[CrossRef](#)]
19. Schneider, J.; Farris, L.; Nolze, G.; Reinsch, S.; Cios, G.; Tokarski, T.; Thompson, S. Microstructure Evolution in Inconel 718 Produced by Powder Bed Fusion Additive Manufacturing. *J. Manuf. Mater. Process.* **2022**, *6*, 20. [[CrossRef](#)]
20. Fei, J.; Liu, G.; Patel, K.; Özel, T. Effects of Machining Parameters on Finishing Additively Manufactured Nickel-Based Alloy Inconel 625. *J. Manuf. Mater. Process.* **2020**, *4*, 32. [[CrossRef](#)]
21. Wang, J.; Zhu, R.; Liu, Y.; Zhang, L. Understanding melt pool characteristics in laser powder bed fusion: An overview of single- and multi-track melt pools for process optimization. *Adv. Powder Mater.* **2023**, *2*, 100137. [[CrossRef](#)]
22. ASTM E1856-13; Standard Guide for Evaluating Computerized Data Acquisition Systems Used to Acquire Data from Universal Testing Machines. ASTM International: West Conshohocken, PA, USA, 2021.
23. Huang, S.; Chen, B.; Liu, W.; Zhou, B.; Zhang, X.; Zeng, Q.; Guo, S. Effect of Heat Treatment on Microstructure and Properties of GH3536 Fabricated by Selective Laser Melting. *Metals* **2022**, *12*, 1184. [[CrossRef](#)]
24. Liang, J.; He, Z.; Du, W.; Ruan, X.; Guo, E.; Shen, N. Tailoring the microstructure and mechanical properties of laser metal-deposited Hastelloy X superalloy sheets via post heat-treatment. *Mater. Sci. Eng. A* **2023**, *884*, 145546. [[CrossRef](#)]
25. Haack, M.; Kuczyk, M.; Seidel, A.; López, E.; Brückner, F.; Leyens, C. Investigation on the formation of grain boundary serrations in additively manufactured superalloy Haynes 230. *J. Laser Appl.* **2020**, *32*, 032014. [[CrossRef](#)]
26. Wang, H.; Wu, H.; Liu, Y.; Qiu, W.; Deng, H.; Zhou, L.; Chen, L. Oxidation Behavior of Hastelloy X Alloy Fabricated by Selective Laser Melting and Subsequent Hot Isostatic Pressing Treatment. *Adv. Eng. Mater.* **2022**, *24*, 2200369. [[CrossRef](#)]
27. Montero-Sistiaga, M.L.; Pourbabak, S.; Van Humbeeck, J.; Schryvers, D.; Vanmeensel, K. Microstructure and mechanical properties of Hastelloy X produced by HP-SLM (high power selective laser melting). *Mater. Des.* **2019**, *165*, 107598. [[CrossRef](#)]

28. Montero-Sistiaga, M.L.; Liu, Z.; Bautmans, L.; Nardone, S.; Ji, G.; Kruth, J.-P.; Van Humbeeck, J.; Vanmeensel, K. Effect of temperature on the microstructure and tensile properties of micro-crack free hastelloy X produced by selective laser melting. *Addit. Manuf.* **2020**, *31*, 100995. [[CrossRef](#)]
29. Wang, Y.; Li, Y.; Yu, W.; Tang, H.; Wang, H.; Xu, G.; Wang, Z. Effect of a special thermo-mechanical treatment process on microstructure and properties of 7185 alloy. *J. Alloys Compd.* **2023**, *935*, 168072. [[CrossRef](#)]
30. Tillmann, W.; Schaak, C.; Nellesen, J.; Schaper, M.; Aydinöz, M.u.; Hoyer, K.-P. Hot isostatic pressing of IN718 components manufactured by selective laser melting. *Addit. Manuf.* **2017**, *13*, 93–102. [[CrossRef](#)]
31. Peters, M.; Brodie, E.G.; Thomas, S.; Djumas, L.; Brameld, M.; Salasi, M.; Quadir, Z.; Iannuzzi, M.; Wang, J.; Sercombe, T.; et al. On the importance of nano-oxide control in laser powder bed fusion manufactured Ni-based alloys to enhance fracture properties. *Materialia* **2023**, *32*, 101958. [[CrossRef](#)]

Disclaimer/Publisher's Note: The statements, opinions and data contained in all publications are solely those of the individual author(s) and contributor(s) and not of MDPI and/or the editor(s). MDPI and/or the editor(s) disclaim responsibility for any injury to people or property resulting from any ideas, methods, instructions or products referred to in the content.